ORIGINAL ARTICLE

lajss.org© Latin American Journal of Solids and Structures

www.lajss.org

# Theoretical and Experimental Study of Shaped Charge Jet Penetration into Frozen Soil at Different Temperatures

**Guanghao Shi**[a*], **Zhengxiang Huang** [a]

[a] Nanjing University of Science and Technology, School of Mechanical Engineering, Nanjing, Jiangsu, China.
Email: 120101010217@njust.edu.cn, huangyu@mail.njust.edu.cn

* Corresponding author

https://doi.org/10.1590/1679-7825/e9061

## Abstract

To investigate the mechanical behavior of frozen soil subjected to shaped charge jet penetration at different temperatures, a combined theoretical and experimental approach was adopted. In the theoretical part, based on the dynamic cavity expansion model, the dynamic penetration resistance of frozen soil at various temperatures under high-velocity shaped charge jet penetration was calculated by incorporating the constitutive model and equation of state (EOS) for frozen soil. The calculated dynamic penetration resistance was then integrated with the axial penetration model of the shaped charge jet and the radial cavity growth model to determine the penetration cavity profile formed by jet penetration into frozen soil at different temperatures. The dynamic penetration resistance was subsequently validated through experiments on shaped charge jet penetration into frozen soil at −6 °C. The results indicated that as temperature decreases, the dynamic penetration resistance of frozen soil increases significantly, while the cavity diameter decreases markedly. However, no obvious variation was observed in cavity depth.

## Keywords

Frozen soil; Cavity expansion model; Temperature effect; Shaped charge penetration; Dynamic penetration resistance

## Graphical Abstract

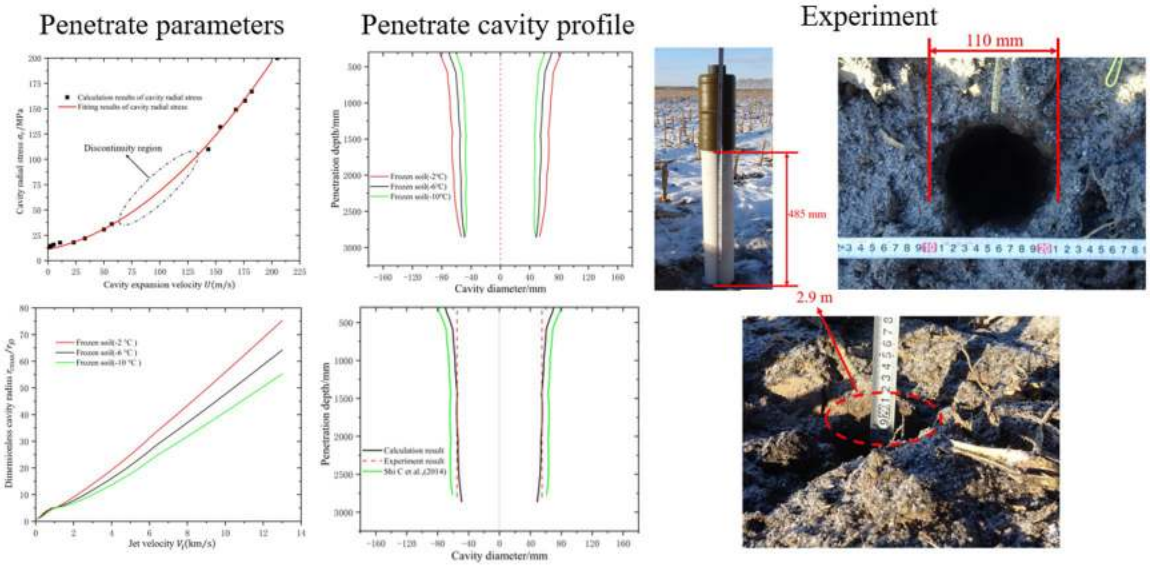


Received April 05, 2026. In revised form April 13, 2026. Accepted May 06, 2026. Available online May 07, 2026.
https://doi.org/10.1590/1679-7825/e9061

Latin American Journal of Solids and Structures. ISSN 1679-7825. Copyright © 2026. This is an Open Access article distributed under the terms of the Creative Commons Attribution License, which permits unrestricted use, distribution, and reproduction in any medium, provided the original work is properly cited.

## 1 INTRODUCTION

Frozen soil is a four-phase composite material comprising solid particles, ice, liquid water, and air. It is estimated that permafrost-affected soils cover approximately 8% of the global land area, while seasonally frozen soil accounts for about 50% (Bockheim et al., 2006). With the advancement of modern underground protective engineering, an increasing number of such structures are being constructed in frozen soil regions. In the field of military weaponry, shaped charge jets offer advantages over traditional kinetic energy warheads, such as platform independence and high penetration velocity, making them widely used in the leading stage of tandem warheads. Therefore, it is essential to evaluate the protective performance of the overburden layer of underground protective structures in frozen soil areas when subjected to shaped charge jet penetration.

Shi G et al. (2026) pointed out that calculating the dynamic resistance of the target is crucial when determining the cavity profile formed by the penetration of a shaped charge jet into non-metallic targets such as soil. The dynamic cavity expansion theory has been widely applied to compute the resistance of various non-metallic targets, including concrete (Luk et al., 1987; Forrestal et al., 1997; He T et al., 2011; Feng J et al., 2015), soil (Forrestal et al., 1992), rock (Forrestal et al., 1981; Forrestal, 1986), sandy soil (Shi C et al., 2014), and ceramics (Satapathy, 2001). These studies have provided a relatively solid theoretical foundation for the dynamic cavity expansion theory.

The selection of an appropriate yield criterion (i.e., constitutive model) is essential for establishing a reliable dynamic cavity expansion model. Commonly used yield criteria in existing dynamic cavity expansion models include Tresca (Luk et al., 1987), Drucker–Prager (Feng J et al., 2015), and Mohr–Coulomb (Forrestal et al., 1997; He T et al., 2011; Forrestal et al., 1992; Forrestal, 1986; Shi C et al., 2014). However, existing dynamic cavity expansion models commonly equate yield with failure, assuming that the material remains in an elastic stress state until the failure point is reached. Furthermore, these models typically presume that material compaction and shear behavior are independent during cavity expansion: shear is governed by the yield surface (i.e., the constitutive model), while compaction is described by the EOS. These assumptions, however, do not hold for frozen soil. During the cavity expansion stage in frozen soil, an elastoplastic loading phase exists between the purely elastic loading stage and final yield (KONG et al., 2023). Moreover, a strong coupling between compaction and shear is clearly observed throughout the loading process. This indicates that the yield criteria adopted in current dynamic cavity expansion models are inadequate for characterizing the dynamic resistance of frozen soil under penetration loading.

Recognizing the limitations of traditional cavity expansion methods in evaluating the dynamic resistance of frozen soil, this study adopts the modified unified hardening (UH) model, which accounts for cryogenic intergranular suction (KONG et al., 2023), together with a three-stage EOS for frozen soil. This combined approach is used to calculate the dynamic resistance of frozen soil at different temperatures during shaped charge jet penetration. After obtaining the dynamic resistance values, the penetration parameters and cavity profiles resulting from jet penetration into frozen soil at various temperatures are determined by combining the axial penetration model and the radial cavity expansion model for shaped charge jets proposed by Shi G et al. (2026). Meanwhile, the dynamic resistance models for frozen soil at different temperatures are experimentally validated, and the influence of frozen soil temperature on both the dynamic resistance of frozen soil and the jet penetration behavior is further analyzed.

## 2 Constitutive Models and EOS for Frozen Soil

Wood (1990) proposed an elastoplastic constitutive model for soil based on energy equations, known as the Modified Cambridge Clay (MCC) model. Prior to the MCC model, soil compaction and shear were generally treated as independent mechanical behaviors. The MCC model was the first to unify these two aspects, laying the foundation for modern soil constitutive modeling. However, in practical engineering applications—including those involving frozen soil—soils often exist in an over-consolidated state due to complex stress histories, a condition that the MCC model cannot adequately describe. To address this limitation, Yao (2015) developed a constitutive model for over-consolidated soil termed the UH model. Although its parameters are identical to those of the MCC model, the UH model can consistently and reasonably capture the complex stress–strain characteristics of over-consolidated soils, such as shear contraction, shear dilatancy, hardening, and softening. Building upon the UH model, KONG et al. (2023) introduced frozen soil temperature as an external variable to account for cryogenic intergranular suction, leading to the development of a modified UH model that integrates cryogenic intergranular suction for frozen soil.

### 2.1 The modified UH model considering cryogenic intergranular suction

In the modified UH model proposed by Yao (2015), two yield surfaces are defined, as illustrated in Figure 1: the current yield surface and the reference yield surface. The current yield surface represents the present stress state of the soil.

The distance between these two surfaces corresponds to the over-consolidation ratio (OCR), with a larger separation indicating a higher OCR value. When the distance reduces to zero, the two surfaces coincide, indicating that the soil has transitioned to a normally consolidated state. The two yield surfaces are associated with distinct hardening parameters. The expression for the reference yield surface is given in Equation (1), that for the current yield surface in Equation (2), and the definition of the OCR is presented in Equation (3).

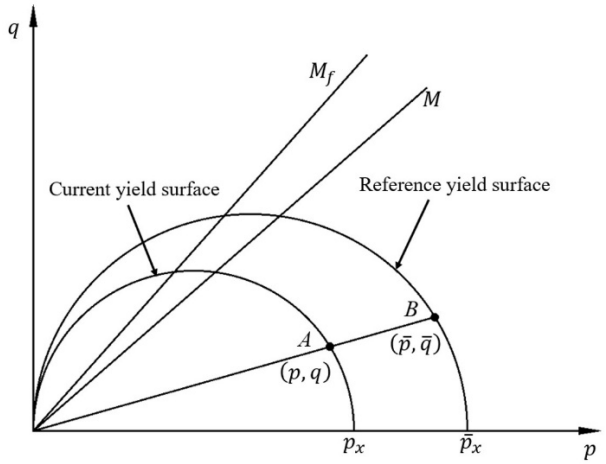


**Figure 1** Current yield surface and reference yield surface.

$$\bar{f} = \ln\frac{\bar{p}}{\bar{p}_x} + \ln\left(1+\frac{\bar{q}^2}{M^2\bar{p}^2}\right) - \frac{1}{c_{\mathrm{p}}}\varepsilon_{\mathrm{v}}^{\mathrm{p}} = 0 \tag{1}$$

$$f = \ln\frac{p}{p_x} + \ln\left(1+\frac{q^2}{M_{\mathrm{f}}^2 p^2}\right) - \frac{1}{c_{\mathrm{p}}}H = 0 \tag{2}$$

$$R = \frac{p}{\bar{p}} = \frac{q}{\bar{q}} \tag{3}$$

where, $\bar{p}$ and $\bar{q}$ are the mean principal stress and generalized shear stress at the reference stress point, respectively; $M$ is the critical state stress ratio; $\bar{p}_x$ is the intersection of the reference yield surface with the mean principal stress axis ($p$-axis). Correspondingly, $p$ and $q$ are the mean principal stress and generalized shear stress at the current stress point; $M_{\mathrm{f}}$ is the ultimate stress ratio; $p_x$ is the intersection of the current yield surface with the $p$-axis. Additionally, $c_{\mathrm{p}} = (\lambda-\kappa)/(1+e_0)$, where $\lambda$ is the slope of the isotropic compression line, $\kappa$ is the slope of the unloading line, $e_0$ is the initial void ratio of the soil, $\varepsilon_{\mathrm{v}}^{\mathrm{p}}$ is the plastic volumetric strain, and $H$ is the hardening parameter of the current yield surface.

Unlike the MCC model (Wood, 1990), which employs the plastic volumetric strain $\varepsilon_{\mathrm{v}}^{\mathrm{p}}$ as the hardening parameter, the modified UH model (Yao, 2015) introduces a unified hardening parameter *H*, as derived in Equation (4), where $\eta = q/p$ is the stress ratio. This parameter is independent of the stress path and is capable of characterizing the hardening behavior of both normally consolidated and over-consolidated soils.

$$H = \int \mathrm{d}H = \int \frac{M_{\mathrm{f}}^4 - \eta^4}{M^4 - \eta^4}\mathrm{d}\varepsilon_{\mathrm{v}}^{\mathrm{p}} \tag{4}$$

Building upon the modified UH model (Yao, 2015), KONG et al. (2023) incorporated the influence of cryogenic intergranular suction $p_{\mathrm{cs}}$ on the mean effective stress $p$ in frozen soil, applying the corresponding corrections as detailed in Equations (5)–(7).

$$p_{\mathrm{cs}} = -\left(\frac{\rho_1 \mathrm{L}}{2}\cot\theta\right)\ln\frac{T+273.15}{T_0+273.15} \tag{5}$$

$$\theta = \frac{T_0 - T}{\theta_{\mathrm{a}} - \theta_{\mathrm{b}}\left(T - T_0\right)}\frac{\pi}{180^{\circ}} \tag{6}$$

$$p' = p + p_{\mathrm{cs}} \tag{7}$$

where, $\rho_1$ is the density of water, $L$ denotes the latent heat of ice melting, and $\theta_{\mathrm{a}}$ and $\theta_{\mathrm{b}}$ are coefficients associated with the type of frozen soil.

The pre-consolidation pressure of frozen soil is also influenced by temperature. KONG et al. (2023) accounted for this effect and introduced corresponding corrections to both the pre-consolidation pressure and the initial cohesion of frozen soil, as expressed in Equations (8) and (9), respectively. Furthermore, building upon the modified UH model (Yao, 2015), they formulated the over-consolidation ratio *R* and the ultimate stress ratio $M_{\mathrm{f}}$ for frozen soil, incorporating the effect of cryogenic intergranular suction as shown in Equations (10) and (11).

$$p_x = p_{x0} + \alpha\ln\frac{T}{T_0} \tag{8}$$

$$c_0 = -c_{0\mathrm{a}}T + c_{0\mathrm{b}} \tag{9}$$

$$R = \frac{\frac{p'}{p_x}\left(1+\eta'^4\right)}{M^2}\exp\left(-\frac{\varepsilon_{\mathrm{v}}^{\mathrm{p}}}{c_{\mathrm{p}}}\right) \tag{10}$$

$$M_{\mathrm{f}} = M + (1-R)\frac{c_0}{p'} \tag{11}$$

where, $p_{x0}$ denotes the pre-consolidation pressure of frozen soil at the reference temperature $T_0$, $p_x$ is the pre-consolidation pressure at temperature $T$, and $\alpha$ is the temperature coefficient for pre-consolidation pressure; $c_0$ represents the initial cohesion of frozen soil at the reference temperature $T_0$, while $c_{0\mathrm{a}}$ and $c_{0\mathrm{b}}$ are coefficients related to the type of frozen soil; $\eta' = q/p'$ is the stress ratio of the current stress state, and $R$ is the current over-consolidation parameter of frozen soil, as defined previously.

### 2.2 Elastoplastic stress-strain relationship in the modified UH model considering cryogenic intergranular suction

During the analysis of jet penetration into frozen soil, the temperature variation within the frozen soil can be neglected due to the extremely short duration of the penetration process. Consequently, the elastoplastic stress–strain incremental relationship presented in Equation (12) is adopted.

$$\begin{bmatrix}\mathrm{d}p' \\ \mathrm{d}q\end{bmatrix} = \begin{bmatrix}K\cdot\mathrm{A}_1 & 3KG\cdot\mathrm{A}_2 \\ 3KG\cdot\mathrm{A}_2 & 3G\cdot\mathrm{A}_3\end{bmatrix}\begin{bmatrix}\mathrm{d}\varepsilon_{\mathrm{v}} \\ \mathrm{d}\varepsilon_{\mathrm{d}}\end{bmatrix} \tag{12}$$

where $\mathrm{d}p'$ denotes the increment of the mean effective principal stress; $\mathrm{d}q$ is the increment of the generalized shear stress; $\mathrm{d}\varepsilon_{\mathrm{v}}$ and $\mathrm{d}\varepsilon_{\mathrm{d}}$ represent the increments of total volumetric strain and total shear strain, respectively. The elastic bulk modulus $K$ and shear modulus $G$ are given by $K = E/[3(1-2\upsilon)]$ and $G = E/[2(1+\upsilon)]$, with $\upsilon$ being the Poisson's ratio of the frozen soil. Parameters $A_1$, $A_2$, and $A_3$ are defined in Equation (13).

$$\begin{cases} \mathrm{A}_1 = \dfrac{\left(M_{\mathrm{f}}^4 - \eta'^4\right)p' + 12G\mathrm{c}_{\mathrm{p}}\eta'^2}{\left(M_{\mathrm{f}}^4 - \eta'^4\right)p' + 12Gc_{\mathrm{p}}\eta'^2 + Kc_{\mathrm{p}}\left(M^2 - \eta'^2\right)^2} \\ \mathrm{A}_2 = \dfrac{-2c_{\mathrm{p}}\left(M^2 - \eta'^2\right)\eta'}{\left(M_{\mathrm{f}}^4 - \eta'^4\right)p' + 12Gc_{\mathrm{p}}\eta'^2 + Kc_{\mathrm{p}}\left(M^2 - \eta'^2\right)^2} \\ \mathrm{A}_3 = \dfrac{\left(M_{\mathrm{f}}^4 - \eta'^4\right)p' + Kc_{\mathrm{p}}\left(M^2 - \eta'^2\right)^2}{\left(M_{\mathrm{f}}^4 - \eta'^4\right)p' + 12\mathrm{G}c_{\mathrm{p}}\eta'^2 + \mathrm{K}c_{\mathrm{p}}\left(M^2 - \eta'^2\right)^2} \end{cases} \tag{13}$$

In the modified UH model for frozen soil that accounts for cryogenic intergranular suction, the elastic volumetric strain is calculated in the same manner as in the MCC model (Wood, 1990), as shown in Equation (14), where $p_0$ denotes the initial mean pressure of the soil, taken as atmospheric pressure. The total volumetric strain $\varepsilon_{\mathrm{v}}$ and total shear strain $\varepsilon_{\mathrm{d}}$ generated in frozen soil during loading each consist of elastic and plastic components, i.e., $\varepsilon_{\mathrm{v}} = \varepsilon_{\mathrm{v}}^{\mathrm{e}} + \varepsilon_{\mathrm{v}}^{\mathrm{p}}$ and $\varepsilon_{\mathrm{d}} = \varepsilon_{\mathrm{d}}^{\mathrm{e}} + \varepsilon_{\mathrm{d}}^{\mathrm{p}}$. Furthermore, based on the radial stress $\sigma_r$ and circumferential stress $\sigma_\theta$ in the spherical coordinate system, the mean stress $p'$ and the generalized shear stress $q$ are defined according to Equations (15) and (16), respectively.

$$\varepsilon_{\mathrm{v}}^{\mathrm{e}} = c_\kappa \ln\frac{p}{p_0} \tag{14}$$

$$p' = \frac{1}{3}\left(\sigma_r + 2\sigma_\theta\right) \tag{15}$$

$$q = \sigma_r - \sigma_\theta \tag{16}$$

As loading proceeds, the stress state of the frozen soil reaches the critical state response region, at which stage its incremental constitutive model is given by Equation (17).

$$\mathrm{d}q = M\mathrm{d}p' \tag{17}$$

In conventional dynamic cavity expansion models, material yield is often equated with failure, implying immediate failure upon reaching the yield state and a purely elastic stress state prior to yielding. However, in reality, the yield of frozen soil does not coincide with failure. As illustrated in Figure 2, before the stress state $(p, q)$ of frozen soil reaches the initial yield surface $f_1$, the material remains elastic. Yielding begins once this surface is reached, initiating an elastoplastic loading stage. During this stage, owing to the over-consolidated nature of frozen soil, dilatancy occurs and the stress state moves beyond the critical state line. With further loading, the over-consolidation effect gradually diminishes, and the stress state slowly returns toward the critical state line. Concurrently, the initial yield surface $f_1$ expands toward the failure surface (final yield surface) $f_2$. The convergence of the stress state to the critical state line together with the evolution of the yield surface signifies the end of the elastoplastic loading stage in frozen soil.

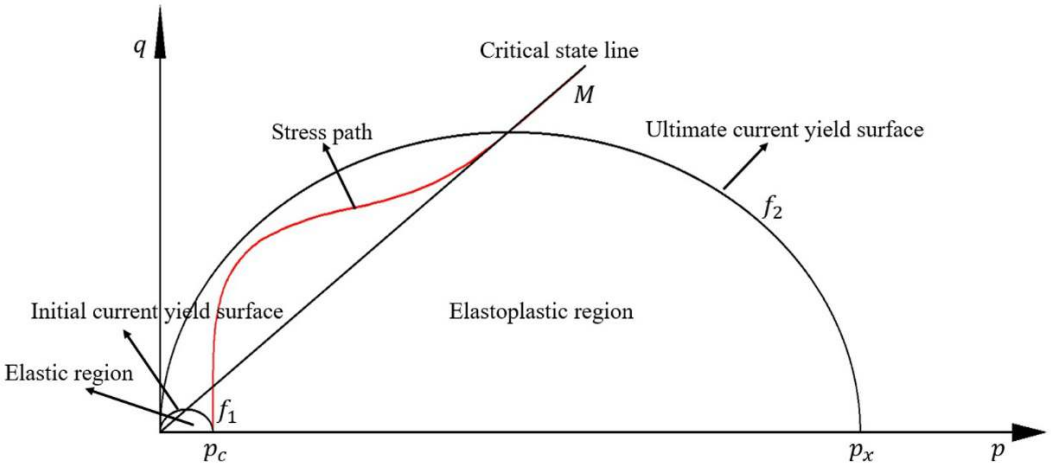


**Figure 2** Stress path during the loading process of frozen soil.

### 2.3 Three-stage EOS of frozen soil

Conventional dynamic cavity expansion models treat material shear and compaction as independent mechanisms, governed separately by the constitutive model and the EOS. However, in frozen soil, shear induces both volumetric strain and shear strain. Consequently, the coupling between shear and compaction must be considered during its loading process. Furthermore, during cavity expansion loading, the EOS for frozen soil—i.e., the pressure-density relationship—can be described in three distinct stages.

In the first stage, corresponding to initial loading, the applied load is relatively low and is primarily carried by the soil skeleton. During this phase, the total volume and void ratio of the frozen soil remain essentially unchanged, and the density can be treated as constant. The expression for density at this stage is given in Equation (18).

$$\rho = \rho_0 \quad p' \le p_c' \tag{18}$$

In the second stage, the frozen soil transitions from the elastic to the elastoplastic loading phase. During this phase, loading induces significant volumetric strain, comprising both dilation and contraction. The total volumetric strain, $\varepsilon_v$, can be computed using the constitutive model described in Section 2.2, and the corresponding density of the frozen soil is determined by Equation (19).

$$\rho = \frac{\rho_0}{1+\varepsilon_v} \quad p_c' \le p' \le p_s' \tag{19}$$

In the third stage, as the second-stage EOS loading proceeds, the pore air within the frozen soil is continuously compressed until it fully dissolves into the pore water. Once the pore air is completely compressed, the second-stage EOS loading concludes and the material transitions to the third-stage EOS. Consequently, the frozen soil changes from a four-phase to a three-phase mixture, marking the end of pore collapse. At this point, the pressure–density relationship of the frozen soil is governed by the Murnaghan EOS for the resulting mixture, as expressed in Equation (20).

$$\rho = \rho_s \left( \frac{p' - p_s'}{A} + 1 \right)^{\frac{1}{n}} \quad p_s' \le p' \tag{20}$$

where $p'$ denotes the current pressure, $p_s'$ is the fully compacted pressure, and $p_c'$ represents the initial compaction pressure; $\rho_0$ is the initial density of the frozen soil, $\rho_s$ is the fully compacted density, and $\rho$ is the current density. Parameters $A$ and $n$ are the coefficients in the Murnaghan EOS for the three-phase mixture after full compaction.

## 3 Cavity Expansion Response and Governing Equations for Frozen Soil

### 3.1 Cavity expansion response in frozen soil

Under a relatively low cavity expansion velocity $U$, the elastic region is bounded by $r = ct$ and $r = c_d t$, whereas the elastoplastic response region lies between $r = Ut$ and $r = ct$, as illustrated in Figure 3. Here, $r$ is the Eulerian radial coordinate, $t$ denotes time, $c$ is the velocity of the inner boundary of the elastic region, and $c_d$ represents the expansion wave velocity in the elastic region. In this case, the elastoplastic response is governed by the modified UH model for frozen soil that incorporates cryogenic intergranular suction (Equation (12)) and the pore-collapse EOS (Equation (19)).

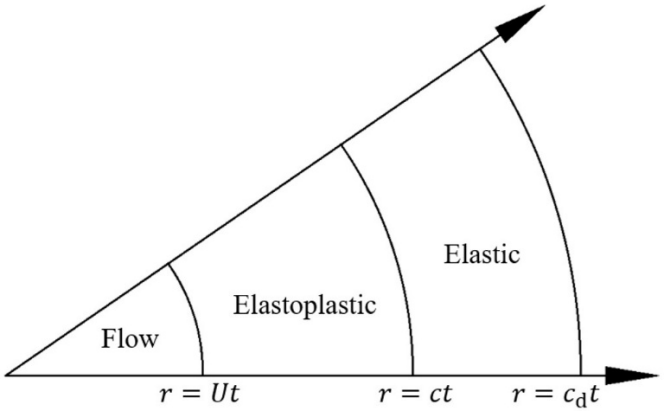


**Figure 3** The Elastic-Elastoplastic response model.

As the cavity expansion velocity $U$ increases, the interface velocity $c$ between the elastic and elastoplastic regions rises correspondingly (Figure 3). This leads to the direct formation of a Hugoniot jump at that interface, followed by entry into the critical state region, as illustrated in Figure 4. In the critical state, the pores within the frozen soil remain partially uncompacted, and the mechanical response is governed jointly by the critical state constitutive model for frozen soil (Equation (17)) and the pore-collapse EOS (Equation (19)).

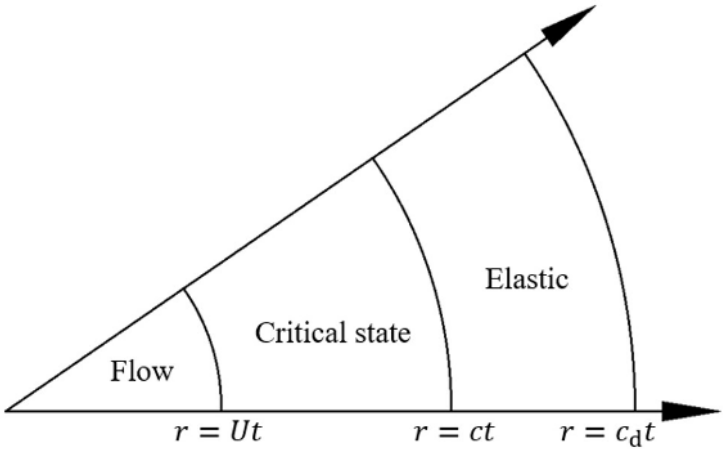


**Figure 4** The Elastic-Critical state response model.

As the cavity expansion velocity increases further, the air within the frozen soil becomes fully compressed during the loading process in the critical state response region (Figure 4). Consequently, the critical state region transitions into a fully dense critical state region, as depicted in Figure 5. In this fully dense critical state region, the constitutive model remains the same as that of the critical state region (Equation (17)), while the EOS switches to the compaction EOS for frozen soil (Equation (20)).

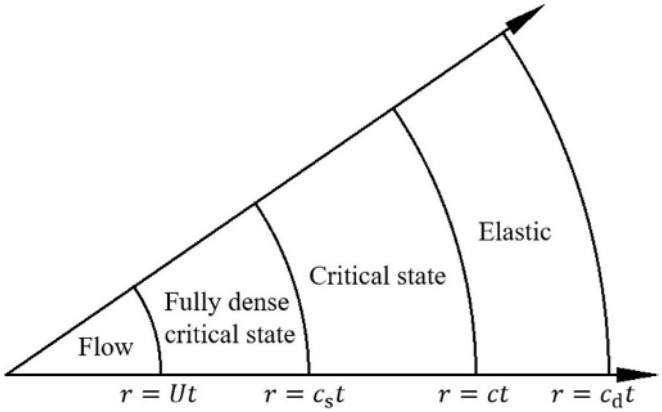


**Figure 5** The Fully dense critical state-Critical state-Elastic response.

At higher cavity expansion velocities $U$, the interface velocity $c$ attains a correspondingly elevated value. Under this condition, the elastic region undergoes a direct transition into the fully dense critical state region via a Hugoniot jump. The corresponding cavity expansion response process is illustrated in Figure 6.

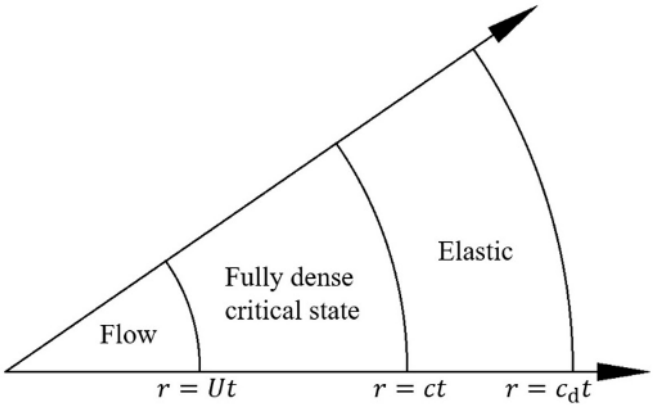


**Figure 6** The Fully dense critical state-Elastic response.

### 3.2 Conservation equations for cavity expansion

For a spherically symmetric cavity expansion, the average stress $p'$ and shear stress $q$ can be obtained from the radial stress $\sigma_r$ and circumferential stress $\sigma_\theta$ using Equations (15) and (16), respectively. Correspondingly, the volumetric strain $\varepsilon_{\mathrm{v}}$ and shear strain $\varepsilon_{\mathrm{d}}$ can be derived from the radial strain $\varepsilon_r$ and circumferential strain $\varepsilon_\theta$ through Equations (21) and (22).

$$\varepsilon_{\mathrm{v}} = \varepsilon_r + 2\varepsilon_\theta \tag{21}$$

$$\varepsilon_{\mathrm{d}} = \frac{2}{3}\left(\varepsilon_r - \varepsilon_\theta\right) \tag{22}$$

Based on the strain-displacement relationship, the radial strain $\varepsilon_r$ and circumferential strain $\varepsilon_\theta$ are given by Equations (23) and (24), respectively.

$$\varepsilon_r = \frac{\partial u}{\partial r} \tag{23}$$

$$\varepsilon_\theta = -\frac{u}{r} \tag{24}$$

In this study, the symbol d denotes the time derivative operator, defined in Equation (25).

$$\mathrm{d}(\ ) = \frac{\partial(\ )}{\partial t} + V\frac{\partial(\ )}{\partial r} \tag{25}$$

where $V$ is the particle radial velocity, and $\partial(\ )/\partial t$ denotes the local time derivative.

In the Eulerian spherically symmetric coordinate system, the conservation equations are given by Equations (26) and (27) (Shi C et al., 2014).

$$\frac{\partial \sigma_r}{\partial r} + \frac{2\left(\sigma_r - \sigma_\theta\right)}{r} = -\rho\left(\frac{\partial V}{\partial t} + V\frac{\partial V}{\partial r}\right) \tag{26}$$

$$\rho\left(\frac{\partial V}{\partial r} + \frac{2V}{r}\right) = -\left(\frac{\partial \rho}{\partial t} + V\frac{\partial \rho}{\partial r}\right) \tag{27}$$

By combining Eqs. (15) and (16), the momentum conservation equation (Eq. 26) can be reformulated in terms of the average stress $p'$ and the generalized shear stress $q$, yielding Eq. (28).

$$\frac{\partial p'}{\partial r} + \frac{2}{3}\frac{\partial q}{\partial r} + \frac{2q}{r} = -\rho\left(\frac{\partial V}{\partial t} + V\frac{\partial V}{\partial r}\right) \tag{28}$$

The dimensionless transformation method proposed by Forrestal et al. (1997) is adopted in this study, as expressed in Equation (29).

$$\xi = \frac{r}{ct};\xi_s = \frac{r}{c_s t};\overline{u} = \frac{u}{ct};\overline{V} = \frac{V}{c};\epsilon = \frac{U}{c} \tag{29}$$

The momentum conservation equation (Equation (28)) and the mass conservation equation (Equation (27)) can then be transformed into their dimensionless forms, yielding Equations (30) and (31), respectively.

$$\frac{\mathrm{d}p'}{\mathrm{d}\xi} + \frac{2}{3}\frac{\mathrm{d}q}{\mathrm{d}\xi} + 2\frac{q}{\xi} = -\rho c^2(\overline{V} - \xi)\frac{\mathrm{d}\overline{V}}{\mathrm{d}\xi} \tag{30}$$

$$\frac{\mathrm{d}\overline{V}}{\mathrm{d}\xi} = -\frac{2\overline{V}}{\xi} + \frac{1}{\rho}(\xi - \overline{V})\frac{\mathrm{d}\rho}{\mathrm{d}\xi} \tag{31}$$

### 3.3 Governing equations of the response region

As described in Section 3.1, the cavity expansion response mode evolves with increasing cavity velocity. During the loading process in frozen soil, four distinct response regions emerge: the elastic region, the elastoplastic region, the critical state region, and the fully dense critical state region. This section derives the governing equations for each of these four response regions.

#### 3.3.1 Elastic region response

The constitutive model for the elastic response region follows the generalized Hooke's law. In this study, stress is defined as positive in compression, whereas strain is taken as negative. The constitutive relations for the elastic region are given by Equations (32) and (33).

$$\mathrm{d}p' = -K\varepsilon_{\mathrm{v}} \tag{32}$$

$$\mathrm{d}q = -3G\varepsilon_{\mathrm{d}} \tag{33}$$

where $K$ is the bulk modulus and $G$ is the shear modulus.

By combining Equations (32) and (33) with Equations (21)-(24) and making them dimensionless, the dimensionless constitutive equations for the elastic response region can be derived, as given in Equations (34) and (35).

$$\frac{\mathrm{d}p'}{\mathrm{d}\xi} = -\frac{K}{\bar{V}-\xi}\left(\frac{\mathrm{d}\bar{V}}{\mathrm{d}\xi} + 2\frac{\bar{V}}{\xi}\right) \tag{34}$$

$$\frac{\mathrm{d}q}{\mathrm{d}\xi} = -\frac{2G}{\bar{V}-\xi}\left(\frac{\mathrm{d}\bar{V}}{\mathrm{d}\xi} - \frac{\bar{V}}{\xi}\right) \tag{35}$$

Combining the dimensionless constitutive equations for the elastic region (Equations (34) and (35)) with the dimensionless momentum conservation equation (Equation (30)) yields the ordinary differential equation (ODE) given in Equation (36). This equation contains only one ordinary differential term, $\mathrm{d}\bar{V}/\mathrm{d}\xi$, and can be solved numerically under appropriate boundary conditions.

$$-\frac{K}{\bar{V}-\xi}\left(\frac{\mathrm{d}\bar{V}}{\mathrm{d}\xi} + 2\frac{\bar{V}}{\xi}\right) - \frac{2}{3}\frac{2G}{\bar{V}-\xi}\left(\frac{\mathrm{d}\bar{V}}{\mathrm{d}\xi} - \frac{\bar{V}}{\xi}\right) + 2\frac{q}{\xi} = -\rho c^2(\bar{V}-\xi)\frac{\mathrm{d}\bar{V}}{\mathrm{d}\xi} \tag{36}$$

Based on the incompressibility assumption for the elastic region introduced in Section 2.3, the volumetric strain is assumed to remain zero throughout the loading process. Consequently, the following condition is applied in the solution for the elastic response region:

As previously assumed, the volumetric strain in the elastic region approaches zero, i.e., $\mathrm{d}\bar{V}/\mathrm{d}\xi + 2\bar{V}/\xi \to 0$, which consequently requires the dimensionless particle velocity $\bar{V}$ in this region to approach zero as well.

Based on the assumption that the bulk modulus in the elastic region approaches infinity ($K \to \infty$) and that the condition $\mathrm{d}\bar{V}/\mathrm{d}\xi + 2\bar{V}/\xi \to 0$ holds, substitution into Equation (36) yields $\mathrm{d}p'/\mathrm{d}\xi \neq 0$. As a result, the mean stress $p'$ in the elastic region increases from the initial atmospheric pressure $p_0'$ to the initial yield pressure $p_{\mathrm{c}}'$, while the generalized shear stress remains identically zero ($q \equiv 0$) throughout the loading process. The elastic wave propagation velocity can be calculated from Equation (37), leading to an infinite elastic wave velocity, i.e., $C_{\mathrm{d}} \to \infty$.

$$c_{\mathrm{d}}^2 = \frac{E(1-v)}{(1+v)(1-2v)\rho_0} = \frac{3K(1-v)}{(1+v)\rho_0} \tag{37}$$

### 3.3.2 Elastoplastic region response

By combining the modified UH constitutive model for frozen soil considering cryogenic intergranular suction (Equation (12)) with Equations (21)-(24) and rendering them dimensionless, the corresponding dimensionless form of this constitutive model is obtained, as given by Equations (38) and (39).

$$\frac{\mathrm{d}p'}{\mathrm{d}\xi} = \left[\frac{K\mathrm{A}_1}{\bar{V}-\xi} + \frac{2K\mathrm{A}_2}{\bar{V}-\xi}\right]\frac{\mathrm{d}\bar{V}}{\mathrm{d}\xi} + \left[\frac{2K\mathrm{A}_1}{\bar{V}-\xi} - \frac{2KG\mathrm{A}_2}{\bar{V}-\xi}\right]\frac{\bar{V}}{\xi} \tag{38}$$

$$\frac{\mathrm{d}q}{\mathrm{d}\xi} = \left[\frac{3KG\mathrm{A}_2}{\bar{V}-\xi} + \frac{2G\mathrm{A}_3}{\bar{V}-\xi}\right]\frac{\mathrm{d}\bar{V}}{\mathrm{d}\xi} + \left[\frac{6KG\mathrm{A}_2}{\bar{V}-\xi} - \frac{2G\mathrm{A}_3}{\bar{V}-\xi}\right]\frac{\bar{V}}{\xi} \tag{39}$$

By combining the dimensionless constitutive equations (Equations (38) and (39)) with the dimensionless momentum conservation equation (Equation (30)), Equation (40) is obtained. This ODE contains only one differential term, $\mathrm{d}\bar{V}/\mathrm{d}\xi$, and can be solved numerically under appropriate boundary conditions.

$$\frac{\left[K\mathrm{A}_1+4K\mathrm{A}_2+\frac{4}{3}G\mathrm{A}_3+\rho c^2(\bar{V}-\xi)^2\right]}{\bar{V}-\xi}\frac{\mathrm{d}\bar{V}}{\mathrm{d}\xi}+\frac{\left[2K\mathrm{A}_1+2KG\mathrm{A}_2-\frac{4}{3}G\mathrm{A}_3\right]}{\bar{V}-\xi}\frac{\bar{V}}{\xi}=-\frac{2q}{\xi} \tag{40}$$

Once $\mathrm{d}\bar{V}/\mathrm{d}\xi$ is obtained from Equation (40), it can be substituted into the dimensionless constitutive models (Equations (38) and (39)) to compute $\mathrm{d}p'/\mathrm{d}\xi$ and $\mathrm{d}q/\mathrm{d}\xi$. Meanwhile, by substituting $\mathrm{d}\bar{V}/\mathrm{d}\xi$ into the dimensionless mass conservation equation (Equation (31)), $\mathrm{d}\rho/\mathrm{d}\xi$ can be determined, which in turn is used in the void ratio equation (Equation (41)) to calculate the void ratio of the frozen soil.

$$\frac{\mathrm{d}e}{\mathrm{d}\xi}=-\frac{(1+e)}{\rho}\frac{\mathrm{d}\rho}{\mathrm{d}\xi} \tag{41}$$

3.3.3 Critical state region response

Within the modified UH constitutive model incorporating cryogenic intergranular suction, the stress state $(p',q)$ reaches the critical state line of frozen soil as loading proceeds. At this stage, the constitutive behavior follows the critical state model given in Equation (17), whose dimensionless form is provided in Equation (42).

$$\frac{\mathrm{d}q}{\mathrm{d}\xi}=M\frac{\mathrm{d}p'}{\mathrm{d}\xi} \tag{42}$$

In the critical state region of frozen soil, pore air is still present. Consequently, cavity expansion loading within this region is initially accompanied by pore collapse. During this process, the volumetric strain of frozen soil comprises both elastic and plastic components, as expressed in Equation (43). Combining Equation (43) with the volumetric strain–density relation $-1/\rho\,\mathrm{d}\rho=\mathrm{d}\varepsilon_\mathrm{v}$ and applying a dimensionless similarity transformation yields Equation (44).

$$\mathrm{d}\varepsilon_\mathrm{v}=\mathrm{d}\varepsilon_\mathrm{v}^\mathrm{e}+\mathrm{d}\varepsilon_\mathrm{v}^\mathrm{p}=\left(c_k+c_\mathrm{p}\right)\frac{1}{p}\mathrm{d}p' \tag{43}$$

$$\frac{\mathrm{d}\rho}{\mathrm{d}\xi}=-\frac{\rho}{p}\left(c_\kappa+c_\mathrm{p}\right)\frac{\mathrm{d}p'}{\mathrm{d}\xi} \tag{44}$$

Combining Equation (44) with the dimensionless momentum conservation equation (Equation (30)) and the dimensionless mass conservation equation (Equation (31)) yields the ordinary differential equation given in Equation (45). This equation contains only the ordinary differential term $\mathrm{d}p'/\mathrm{d}\xi$ and can be solved numerically under appropriate boundary conditions.

$$\left\{1+\frac{2}{3}M+\rho c^2(\bar{V}-\xi)^2\frac{1}{p}\left(c_\mathrm{K}+c_\mathrm{p}\right)\right\}\frac{\mathrm{d}p'}{\mathrm{d}\xi}=\rho c^2(\bar{V}-\xi)\frac{2\bar{V}}{\xi}-2M\frac{p'}{\xi} \tag{45}$$

After $\mathrm{d}p'/\mathrm{d}\xi$ is obtained from Equation (45), the following sequential calculations can be performed. First, substituting $\mathrm{d}p'/\mathrm{d}\xi$ into the constitutive equation for the critical state region (Equation (42)) yields $\mathrm{d}q/\mathrm{d}\xi$. Next, $\mathrm{d}p'/\mathrm{d}\xi$ is substituted into Equation (44) to obtain $\mathrm{d}\rho/\mathrm{d}\xi$. This value is then used in the dimensionless mass conservation equation (Equation (31)) to calculate $\mathrm{d}\bar{V}/\mathrm{d}\xi$. Finally, substituting $\mathrm{d}\rho/\mathrm{d}\xi$ into the dimensionless void ratio equation (Equation (41)) gives $\mathrm{d}e/\mathrm{d}\xi$.

3.3.4 Fully dense critical state region response

In the UH model for frozen soil that incorporates cryogenic intergranular suction, the fully dense critical state region shares the same stress characteristics as the critical state region: both have their stress states $(p', q)$ lying on the critical state line. The primary distinction between them lies in their EOS. The critical state region follows the pore-collapse EOS given in Equation (19), whereas the fully dense critical state region follows the Murnaghan EOS presented in Equation (20), whose dimensionless form is shown in Equation (46).

$$\frac{\mathrm{d}\rho}{\mathrm{d}\xi}=\frac{\rho_{\mathrm{s}}}{An}\left[\frac{p'-p'_{\mathrm{s}}}{A}+1\right]^{\frac{1}{n}-1}\frac{\mathrm{d}p'}{\mathrm{d}\xi} \tag{46}$$

Combining the dimensionless Murnaghan EOS (Equation (46)) with the dimensionless momentum conservation equation (Equation (30)) and mass conservation equation (Equation (31)) yields the ODE given in Equation (47). This equation contains only a single ordinary differential term, $\mathrm{d}p'/\mathrm{d}\xi$, and can therefore be solved numerically under appropriate boundary conditions.

$$\left\{1+\frac{2}{3}M-c^2(\bar{V}-\xi)^2\frac{\rho_{\mathrm{s}}}{An}\left[\frac{p'-p'_{\mathrm{s}}}{A}+1\right]^{\frac{1}{n}-1}\right\}\frac{\mathrm{d}p'}{\mathrm{d}\xi}=\rho c^2(\bar{V}-\xi)\frac{2\bar{V}}{\xi}-2M\frac{p'}{\xi} \tag{47}$$

Once the ordinary differential term $\mathrm{d}p'/\mathrm{d}\xi$ is solved from Equation (47), it can be substituted into the dimensionless constitutive model (Equation (42)) to determine $\mathrm{d}q/\mathrm{d}\xi$. Simultaneously, combining $\mathrm{d}p'/\mathrm{d}\xi$ with the dimensionless Murnaghan EOS (Equation (46)) yields $\mathrm{d}\rho/\mathrm{d}\xi$. This result is then substituted into the dimensionless mass conservation equation (Equation (31)) to calculate $\mathrm{d}\bar{V}/\mathrm{d}\xi$. In the fully dense critical state region, the pore air within the frozen soil has been completely compressed and the soil is fully compacted. Consequently, during cavity expansion loading in this region, the void ratio $e$ of the frozen soil remains constant and equal to the fully compacted void ratio $e_{\mathrm{s}}$.

**3.4 Boundary conditions and solution of cavity response regions**

Figures 3–6 illustrate the cavity expansion response modes of frozen soil under different cavity expansion velocities. Among these modes, four distinct response regions emerge: the elastic region, the elastoplastic region, the critical state region, and the fully dense critical state region. Section 3.3 presents the governing equations for these four regions. To solve these equations, appropriate external boundary conditions—specifically for the variables $p'$, $q$, $\rho$, $e$, and $\bar{V}$—must be provided. Notably, Hugoniot jumps are present in the cavity expansion responses shown in Figures 4–6. This section introduces the boundary conditions for the four response regions as well as the corresponding Hugoniot jump conditions.

3.4.1 Hugoniot jump conditions

In the cavity expansion response modes illustrated in Figures 4–6, the elastic region transitions directly via a Hugoniot jump into either the critical state region or the fully dense critical state region. This jump process always satisfies the mass and momentum conservation equations across the interface, as expressed in Equations (48) and (49).

$$\rho_2\left(V_2-c\right)=\rho_1\left(V_1-c\right) \tag{48}$$

$$\sigma_{r2}+\rho_2V_2\left(V_2-c\right)=\sigma_{r1}+\rho_1V_1\left(V_1-c\right) \tag{49}$$

where subscripts '2' and '1' denote quantities on opposite sides of the interface, and $c$ is the interface velocity.

3.4.2 The initial boundary conditions of the elastic response region's outer boundary

Taking the cavity expansion response mode in Figure 3 as an example, the elastic region is bounded by the outer boundary $r=c_{\mathrm{d}}t$ and the inner boundary $r=ct$. At the outer boundary $\xi=c_{\mathrm{d}}/c$, Section 3.3.1 shows that the velocity $c_{\mathrm{d}}$ tends to infinity; consequently, $\xi$ also approaches infinity at this boundary. Here, the outer boundary condition corresponds to the far-field condition of the frozen soil, as given in Equation (50).

$$p'_{\xi\to\infty} = p_0; q_{\xi\to\infty} = 0; \rho_{\xi\to\infty} = \rho_0; e_{\xi\to\infty} = e_0; \overline{V}_{\xi\to\infty} = 0 \tag{50}$$

where $p_0$ is the atmospheric pressure, $\rho_0$ is the initial density of the frozen soil, and $e_0$ is the initial void ratio of the frozen soil.

3.4.3 The initial boundary conditions of the elastoplastic response region's outer boundary

Using the cavity expansion response mode in Figure 3 as an example, the elastoplastic region is bounded externally by $r = ct$ and internally by $r = Ut$. The interface $r = ct$ represents the boundary between the elastic and elastoplastic regions of the frozen soil. At this interface, the material parameters remain continuous, and no Hugoniot jump occurs. Therefore, the boundary conditions on the outer side of the elastoplastic response region coincide with those on the inner side of the elastic region, as specified in Equation (51).

$$p'_{\xi=1} = p'_{\mathrm{c}}; q_{\xi=1} = 0; \rho_{\xi=1} = \rho_0; e_{\xi=1} = e_0; \overline{V}_{\xi=1} = 0 \tag{51}$$

where $p'_{\mathrm{c}}$ denotes the initial yield pressure of the frozen soil, with all remaining parameters keeping their prior definitions.

3.4.4 The initial boundary conditions of the critical state response region's outer boundary

In the cavity expansion response modes depicted in Figures 4 and 5, a Hugoniot jump occurs at the interface $r = ct$ between the critical state region and the elastic region. The material parameters before the jump are provided by Equation (51). To solve the Hugoniot-jump equations (Equations (48) and (49)), the relationship between pressure and density $(p' - \rho)$ after the jump must be determined.

When a Hugoniot jump occurs from the elastic region to the critical state region of frozen soil, the resulting volumetric strain consists of both elastic and plastic components, i.e., $\varepsilon_{\mathrm{v}} = \varepsilon_{\mathrm{v}}^{\mathrm{e}} + \varepsilon_{\mathrm{v}}^{\mathrm{p}}$. The plastic volumetric strain $\varepsilon_{\mathrm{v}}^{\mathrm{p}}$ can be obtained by solving the constitutive equation for the critical state region (Equation (17)) together with Equation (2), while the elastic volumetric strain $\varepsilon_{\mathrm{v}}^{\mathrm{e}}$ is obtained by solving Equation (17) together with Equation (14)). Consequently, the total volumetric strain induced by the Hugoniot jump is given by Equation (52). According to mass conservation, the post-jump density can then be derived as shown in Equation (53). Finally, by combining the Hugoniot-jump equations, all relevant parameters of the frozen soil after the jump can be calculated.

$$\varepsilon_{\mathrm{v}} = \varepsilon_{\mathrm{v}}^{\mathrm{e}} + \varepsilon_{\mathrm{v}}^{\mathrm{p}} = \frac{\lambda}{1+e_1}\ln\frac{p_2}{p_1} + \frac{\lambda-\kappa}{1+e_1}\ln\left(1+\frac{q_2^2}{M^2 p_2^2}\right) \tag{52}$$

$$\rho_2 = \frac{\rho_1}{1+\varepsilon_{\mathrm{v}}} = \frac{\rho_1}{1+\dfrac{\lambda}{1+e_1}\ln\dfrac{p_1+\rho_1 V_2 c}{\left(1+\dfrac{2}{3}M\right)p_1} + \dfrac{\lambda-\kappa}{1+e_1}\ln 2} \tag{53}$$

3.4.5 The initial boundary conditions of the fully dense critical state response region's outer boundary

The fully dense critical state region appears in the cavity expansion response modes illustrated in Figures. 5 and 6. In Figure 5, at the interface $r = c_{\mathrm{s}}t$ between the critical state region and the fully dense critical state region, the material parameters remain continuous, and no Hugoniot jump occurs. Hence, the outer boundary condition of the fully dense critical state region coincides with the inner boundary condition of the critical state region, as expressed in Equation (54). In the response mode shown in Figure 6, however, a Hugoniot jump takes place directly between the elastic region and the fully dense critical state region. By combining the EOS for the fully dense critical state region (Equation (20)) with the Hugoniot-jump equations (Equations (48) and (49)), the post jump parameters of the frozen soil can be determined.

$$p'_{\xi=c_{\mathrm{s}}/c} = p'_{\mathrm{s}}; q_{\xi=c_{\mathrm{s}}/c} = q_{\mathrm{s}}; \rho_{\xi=c_{\mathrm{s}}/c} = \rho_{\mathrm{s}}; e_{\xi=c_{\mathrm{s}}/c} = e_{\mathrm{s}}; \overline{V}_{\xi=c_{\mathrm{s}}/c} = \overline{V}_{\mathrm{s}} \tag{54}$$

where all parameters retain their prior definitions, with the subscript "s" denoting the state of the frozen soil immediately after compaction.

3.4.6 Termination conditions of cavity expansion

The boundary condition at the cavity surface is given by Equation (55)

$$\bar{V}_{\xi=\epsilon} = \epsilon \tag{55}$$

**3.5 The cavity pressure calculation**

Figures 3–6 illustrate the cavity expansion response modes of frozen soil under different expansion velocities. Section 3.3 introduces the governing equations for each response region, and Section 3.4 provides the corresponding boundary conditions. This section describes the numerical solution procedure for these response models.

3.5.1 The cavity pressure calculation of Figure 3

Cavity pressure refers to the radial pressure acting on the cavity surface. For any given dimensionless cavity expansion velocity $\bar{V}$, there exists a corresponding interface velocity $c$ at the position $\xi = 1$. By prescribing $c$ at $\xi = 1$, Equation (40) can be recursively integrated in the direction of decreasing $\xi$ using the fourth-order Runge–Kutta method, thereby obtaining the distribution of soil parameters $(p'; q; \rho; e; \bar{V})$ along $\xi$. The calculation proceeds until the condition $\bar{V} = \xi$ is satisfied, at which point the particle velocity $V = c\bar{V}$ equals the cavity expansion velocity $U$. Under this condition, the resulting stress state $(p', q)$ corresponds to the stress state at the cavity wall, and the radial stress $\sigma_r$ at the cavity surface can be evaluated using Equations (15) and (16).

3.5.2 The cavity pressure calculation of Figure 4

In the cavity expansion process illustrated in Figure 3, when the interface velocity $c$ exceeds a critical value, Equation (40) fails to yield a convergent solution. This indicates the absence of an elastoplastic response region at such cavity expansion velocities, implying that as the velocity increases, the elastic region will transition directly into the critical state region via a Hugoniot jump, as shown in Figure 4.

For the cavity expansion depicted in Figure 4, the interface velocity $c$ between the elastic and critical state regions is first prescribed. The initial boundary conditions $(p'; q; \rho; e; \bar{V})$ for the critical state region are then obtained following the approach outlined in Section 3.4.4. Subsequently, the governing equations are integrated along decreasing $\xi$ using the fourth-order Runge–Kutta method, yielding the spatial distribution of soil parameters $(p'; q; \rho; e; \bar{V})$. The integration continues until the condition $\bar{V} = \xi$ is satisfied.

3.5.3 The cavity pressure calculation of Figure 5

As the cavity expansion velocity increases, during the numerical solution for the critical state region in Figure 4, the density of the frozen soil reaches its fully compacted density $\rho_s$ before the termination condition $\bar{V} = \xi$ is met. At this stage, the corresponding dimensionless radial coordinate is $\xi = \xi_s$, marking the transition of the frozen soil into the fully dense critical state region. At the interface $\xi = \xi_s$ between the critical state region and the fully dense critical state region, the material parameters remain continuous and no Hugoniot jump occurs. Therefore, the outer boundary conditions of the fully dense region are given by $(p_s'; q_s; \rho_s; e_s; \bar{V}_s)$. Starting from $\xi = \xi_s$, the governing equations for the fully dense critical state region are integrated along decreasing $\xi$ using the fourth-order Runge–Kutta method, yielding the distribution of the soil parameters. The computation terminates when $\bar{V} = \xi$, at which point the particle velocity $V = c\bar{V}$ equals the cavity expansion velocity $U$.

3.5.4 The cavity pressure calculation of Figure 6

As the cavity expansion velocity increases, the elastic region undergoes a Hugoniot jump directly into the fully dense critical state region. Following the approach outlined in Section 3.4.5, the initial boundary conditions for fully dense critical state region can be determined. Combined with the solution procedure for the fully dense critical state region described in Section 3.5.3, the complete response of the region can then be obtained.

3.5.5 Fitting of cavity radial stress

For all cavity expansion response modes, the radial stress $\sigma_r$ acting on the cavity surface and the cavity expansion velocity $U$ can be correlated using the empirical formula proposed by Forrestal et al. (1997), as expressed in Equation (56).

$$\sigma_r = aU^2 + bU + c \tag{56}$$

where $a$, $b$, and $c$ are fitting coefficients, $\sigma_r$ denotes cavity radial stress, and $U$ represents cavity expansion velocity.

## 4 Experiment

The theory presented in Section 3 will be validated through shaped-charge jet penetration experiment on frozen soil. The evaluation will be based on the depth and diameter of the cavity formed in the frozen soil under high-velocity penetration. The jet formation characteristics, including its velocity, length, and diameter, will be determined via two-dimensional numerical simulation using LS-DYNA. This section describes the experimental setup and procedures in detail.

### 4.1 The structure of shaped charge and jet formation

The shaped charge is constructed with a liner made of high-conductivity oxygen-free copper. Its configuration and dimensions are illustrated in Figure 7, which includes a wave-shaper. The charge has a diameter of 125 mm and employs 8701 explosive with a density of 1.717 g/cm$^3$ and a detonation velocity of 8350 m/s.

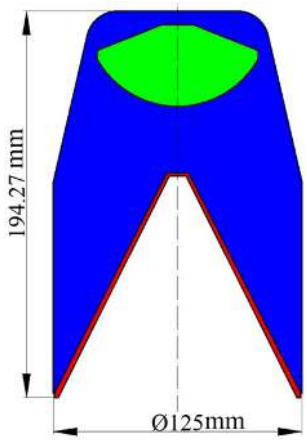


**Figure 7** Schematic of the 125 mm Diameter Shaped Charge Configuration.

The formation parameters of the shaped charge jet are determined through two-dimensional numerical simulations using LS-DYNA. Following the approach of Zhu Q et al. (2020), a mesh size of 0.25 mm is adopted for the jet formation simulation. The resulting jet parameters are summarized in Table 1, and the profile of the formed jet at the tested stand-off distance is shown in Figure 8.

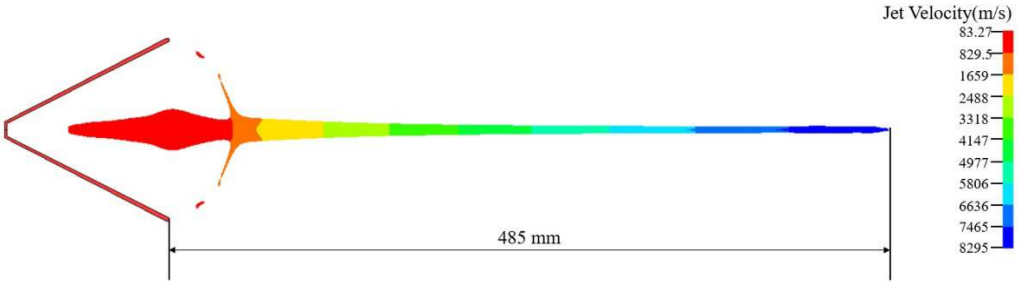


**Figure 8** The simulation of jet forming parameter.

**Table 1** Forming parameters of the 125 mm diameter shaped charge jet.

| Shaped charge diameter/mm | Time/us | Jet tip Velocity/m·s$^{-1}$ | Jet tip diameter/mm | Jet tail Velocity/m·s$^{-1}$ | Jet tail diameter/mm |
|---|---|---|---|---|---|
| 125 | 95 | 8735 | 2.5 | 800 | 19.04 |

### 4.2 Experimental setup and results

The penetration test of frozen soil by a shaped-charge jet was conducted at a temperature of −6°C with a stand-off distance of 485 mm. The charge was initiated at the center of its top surface using a No. 8 electric detonator. After the test, the depth and diameter of the penetration cavity formed by the jet were measured. The experimental results are summarized in Table 2 and illustrated in Figure 9.

**Table 2** Experimental results.

| Shaped charge diameter/mm | Temperature/°C | Stand-off distance/mm | Cavity depth/m | Entrance cavity diameter/mm |
|---|---|---|---|---|
| 125 | -6 | 485 | 2.9 | 110 |

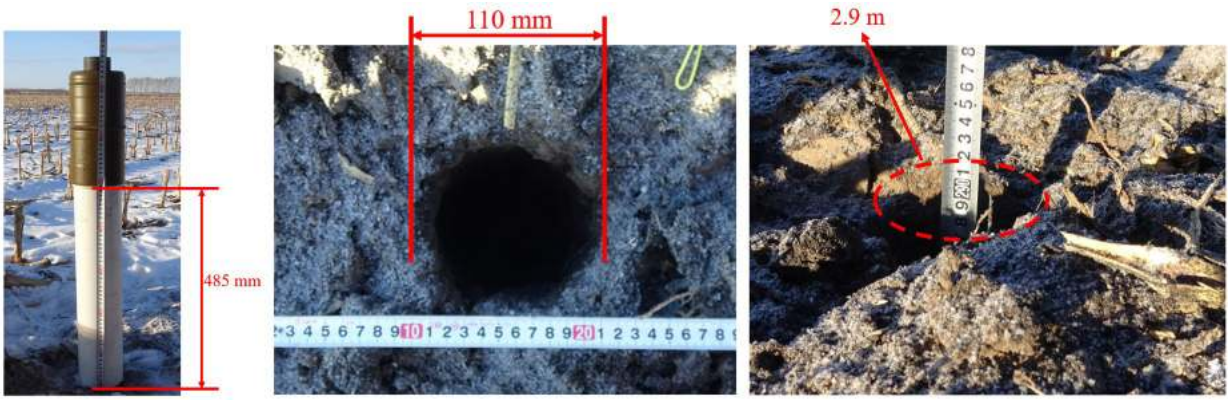


**Figure 9** Experimental Setup and results.

## 5 Results

### 5.1 Material parameters of frozen soil

In the experiment described in Section 4, the moisture content of the frozen soil was determined to be approximately 10% using the oven-drying method, and its dry density was about 1.7534 g/cm$^3$, corresponding to an initial void ratio of $e_0 = 0.54$. The ice content of the frozen soil at different temperatures can be calculated using Equation (57). The four-phase composition of the soil at three selected temperatures is summarized in Table 3. Based on the findings of KONG et al. (2023), the basic parameters of the modified UH model that accounts for cryogenic intergranular suction in the tested frozen soil are listed in Table 4.

$$w = 11.42 \mid T \mid^{-0.62} \tag{57}$$

where $w$ denotes the unfrozen water content in frozen soil, and $T$ denotes the current temperature.

**Table 3** The four-phase composition of frozen soil(1cm$^3$).

| Temperature (%) | Soil particle(mass(g) and Volume(cm$^3$)) | Pore water(mass(g) and Volume(cm$^3$)) | Pore ice(mass(g) and Volume(cm$^3$)) | Pore air(mass(g) and Volume(cm$^3$)) |
|---|---|---|---|---|
| -2 | 1.7534 g/0.6494 cm$^3$ | 0.1303 g/0.1303 cm$^3$ | 0.0405 g/0.045 cm$^3$ | 0 g/0.1753 cm$^3$ |
| -6 | | 0.0659 g/0.0659 cm$^3$ | 0.0985 g/0.1094 cm$^3$ | |
| -10 | | 0.0481 g/0.0481 cm$^3$ | 0.1145 g/0.1272 cm$^3$ | |

**Table 4** Basic Parameters of the Modified UH Model for Frozen Soil with Cryogenic Intergranular Suction.

| $\lambda$ | $\kappa$ | $M$ | $p_c'$/MPa | $\theta_a$ | $\theta_b$ | $\alpha$ | $k/(\mathrm{MPa}\cdot\mathrm{C}^{-1})$ | $k_0$/MPa |
|---|---|---|---|---|---|---|---|---|
| -0.055 | -0.018 | 1.30 | 8.99 | 0. 004 | 0. 014 | 7. 27 | 0. 055 | 0. 73 |

As a four-phase mixture, frozen soil transforms into a three-phase system consisting of soil particles, pore water, and pore ice after full compaction, during which the pore air becomes completely dissolved in the pore water. The Murnaghan EOS parameters for this compacted mixture can be calculated from the corresponding parameters of its individual components using the mixture EOS (Equation (58)) (Bragov et al., 2018). Once the mixture parameters $A$ and $n$ are determined, the initial sound speed $c_0$ and the Hugoniot parameter $\gamma$ of the mixture can be obtained via Equation (59). In this study, the compressibility of the jet is also described by the Murnaghan EOS; all relevant parameters are summarized in Table 5.

$$\rho = \sum_{i=1}^{3} \alpha_i \rho_s \left( \frac{p' - p'_s}{A_i} + 1 \right)^{\frac{1}{n_i}}, i = 1,2,3 \tag{58}$$

$$\gamma = \frac{n+1}{4}, c_0 = \sqrt{\frac{An}{\rho_s}} \tag{59}$$

where $\alpha_i$ denotes the volume fraction of each component in the compacted frozen soil, calculated from the four-phase composition of frozen soil at different temperatures given in Table 3.

**Table 5** The parameters of Murnaghan EOS.

| Materials | Initial sound speed $c_0(\mathrm{km/s})$ | Hugoniot parameter $\gamma$ | Murnaghan parameter $A(\mathrm{GPa})$ | Murnaghan parameter $n$ |
|---|---|---|---|---|
| Soil particle | 4.5 | 1 | 18.2250 | 3 |
| Water | 1.5 | 2 | 0.3214 | 7 |
| ice | 3.23 | 1 | 3.1299 | 3 |
| Frozen soil (-2°C) | 4.0596 | 1.0862 | 11.4959 | 3.3448 |
| Frozen soil (-6°C) | 4.0895 | 1.0429 | 12.2626 | 3.1716 |
| Frozen soil (-10°C) | 4.0997 | 1.0315 | 12.4915 | 3.1260 |
| Jet | 3.92 | 1.488 | 27.7104 | 4.952 |

Using the frozen soil parameters at different temperatures listed in Tables 4 and 5, together with the dynamic cavity expansion theory presented in Section 3, the relationship between the radial stress $\sigma_r(\mathrm{MPa})$ of the cavity and the cavity expansion velocity $U(\mathrm{m/s})$ in frozen soil at various temperatures can be computed. The calculated results are fitted according to Equation (56), with the corresponding fitting coefficients provided in Table 6. Figure 10 displays the fitted curve of radial stress $\sigma_r(\mathrm{MPa})$ versus cavity expansion velocity $U(\mathrm{m/s})$ for frozen soil at −6 °C, where a “discontinuous region” caused by the Hugoniot jump is clearly visible.

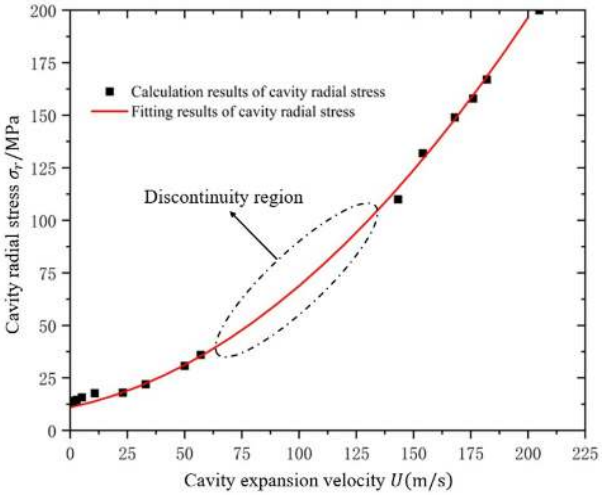


**Figure 10** Fitted $\sigma_r(\mathrm{MPa}) - U(\mathrm{m/s})$ Relationship for Frozen Soil at −6 °C.

**Table 6** The fitting curve of $\sigma_r(\mathrm{MPa}) - U(\mathrm{m/s})$ for frozen soil.

| The temperature of frozen soil/°C | $a$ | $b$ | $c$ |
|---|---|---|---|
| -2 | 0.004 | 0.0027 | 8.4267 |
| -6 | 0.0035 | 0.2277 | 11.0179 |
| -10 | 0.0039 | 0.052 | 20.5874 |

## 5.2 Calculation of penetration parameters and cavity profile

### 5.2.1 Penetration parameters

Based on the parameters presented in Section 5.1, and in conjunction with the modified four-stage axial penetration model and the radial cavity growth model that accounts for compressibility and shock wave effects, as established by Shi G et al. (2026), the axial penetration velocity $u_c$, the stagnation pressure $p_c$, and the maximum dimensionless cavity radius $r_{c,max}/r_{j0}$ are calculated for various jet velocities $V_j$ when the jet penetrates frozen soil at different temperatures. Finally, the cavity profiles formed by the jet penetrating frozen soil at different temperatures are determined.

Taking jet penetration into frozen soil at −6 °C as an example, the resulting axial penetration velocity $u_c$ and stagnation pressure $p_c$ for different jet velocities $V_j$ are presented in Figure 11. Corresponding to the four axial penetration stages shown in Figure 11, the radial cavity growth during jet penetration into frozen soil also exhibits four distinct stages, as illustrated in Figure 12.

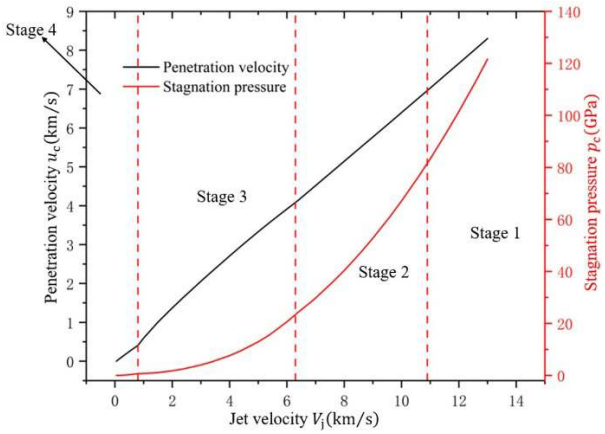


**Figure 11** Penetration Velocity $u_c$ and Stagnation Pressure $p_c$ with Jet Velocity $V_j$ for Frozen Soil at −6 °C.

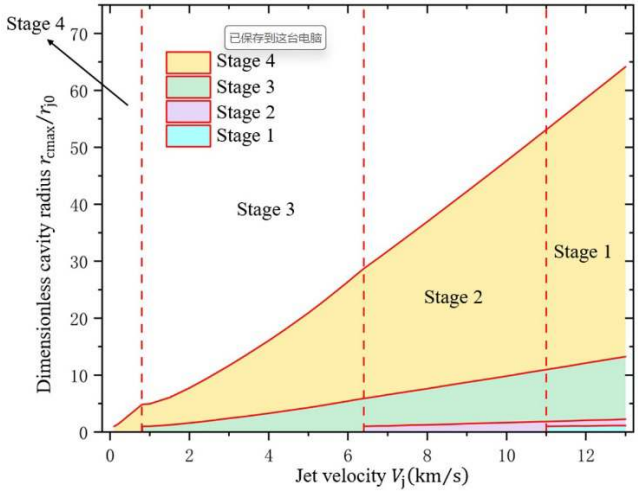


**Figure 12** Dimensionless Cavity Radius at Each Stage of Jet Penetration into −6 °C Frozen Soil.

By combining the data in Table 1 and Figure 8, it can be inferred that Stages 1 and 4 do not occur during the actual axial penetration process of the jet into frozen soil. However, in the context of radial cavity growth, the low-velocity growth stage (Stage 4) is always present.

Moreover, Figure 12 indicates that during cavity expansion, the contribution of the low-velocity growth stages (Stages 3 and 4) to the final cavity radius is significantly greater than that of the high-velocity stages (Stages 1 and 2). This suggests that the overall cavity profile is predominantly shaped by the later, slower growth phases. Furthermore, Figure 13 presents the relationship between the dimensionless maximum cavity radius $r_{c,max}/r_{j0}$ and the jet velocity $V_j$ for frozen soil at different temperatures. It can be observed that as the temperature decreases, the dimensionless maximum cavity radius $r_{c,max}/r_{j0}$ formed under the same jet velocity decreases significantly.

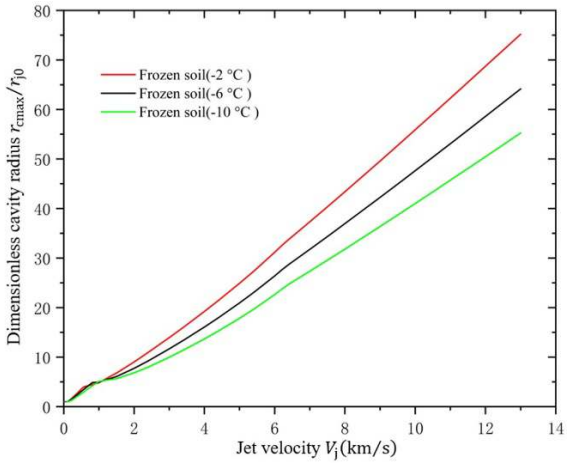


**Figure 13** Dimensionless cavity radius of jet penetration into frozen soil at different temperatures.

### 5.2.2 Cavity profile

Based on the axial penetration analysis of jets in frozen soil at different temperatures and the dimensionless cavity radius results obtained from jet penetration (Section 5.2.1), the cavity profiles formed by jet penetration into frozen soil at various temperatures were calculated using the virtual origin theory of jet formation. The results are presented in Figure 14. These results indicate that as the temperature of the frozen soil decreases, the diameter of the penetration cavity decreases. In contrast, the axial penetration depth remains almost unchanged across different temperatures, suggesting that temperature has only a minor effect on penetration depth.

This study attributes the temperature-dependent behavior mainly to two factors. First, temperature variation alters the cryogenic intergranular suction in frozen soil, which changes its over-consolidation ratio and significantly affects the cavity expansion stress calculated in Section 3 (see Table 6). Second, temperature changes the ice content of the frozen soil, thereby modifying its density and the EOS in the fully compacted state (see Tables 3 and 5). Compared with the pronounced influence on cavity-expansion stress, the effect of temperature on density and the fully compacted state EOS is relatively small. Consequently, differences in the penetration cavities formed by shaped-charge jets in frozen soil at different temperatures are manifested primarily in cavity diameter, rather than in penetration depth.

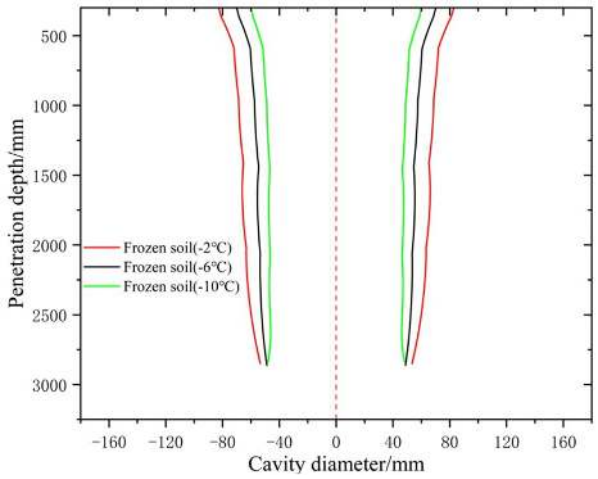


**Figure 14** Cavity Profile from Jet Penetration into Frozen Soil at Different Temperatures.

To validate the model proposed in this study, the calculated cavity profiles are compared with the experimental results of jet penetration into −6 °C frozen soil. Additionally, the cavity profiles are also computed using the cavity expansion model developed by Shi C et al. (2014) combined with the axial penetration and radial cavity growth models presented in this paper. The model of Shi C et al. (2014) neglects the elastoplastic response region between the critical state region and the elastic region during soil cavity expansion and equates the yield of frozen soil with failure. As shown in the comparison results in Figure 15, the model established in this study demonstrates better agreement with the experimental data and is therefore more suitable for analyzing jet penetration into frozen soil.

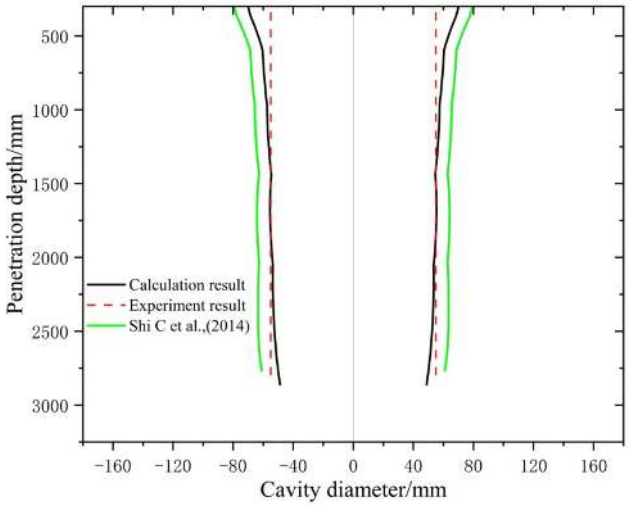


**Figure 15** Comparison of Computational Results and Experimental Data for the Cavity Profiles of Jet Penetration into -6 °C Frozen Soil with Different Models.

## 6 CONCLUSION

A temperature-dependent dynamic cavity expansion model for frozen soil is established based on the modified UH model incorporating cryogenic intergranular suction and the three-stage EOS. The proposed cavity expansion model accounts for the Hugoniot discontinuity that arises in the cavity expansion response region of frozen soil as the cavity expansion velocity increases. Using the material parameters of frozen soil, the dynamic penetration resistance of frozen soil at different temperatures is calculated. The calculated dynamic resistance is substituted into the axial penetration model and radial cavity growth model of shaped charge jets to solve for penetration parameters under jet penetration into frozen soil at different temperatures. Finally, combined with the virtual origin theory of shaped charge jets, the penetration cavity profile induced by jet penetration into frozen soil at various temperatures is calculated.

Further analysis of the cavity profiles formed by jet penetration into frozen soil at different temperatures reveals that temperature has a relatively minor influence on penetration depth; the primary distinction in cavity profiles lies in the cavity diameter. This study attributes the temperature dependent mechanical behavior of frozen soil to two principal mechanisms: First, temperature variations alter the cryogenic intergranular suction, which modifies the over-consolidation parameters and consequently affects the strength of frozen soil; Second; temperature changes the ice content, leading to variations in soil density and the compaction EOS. The influence of temperature through the first mechanism is significantly greater than that through the second. Consequently, differences in cavity profiles resulting from jet penetration into frozen soil at different temperatures are manifested predominantly in cavity diameter rather than in penetration depth.

## Acknowledgments

This research was supported by the Open Research Fund of State Key Laboratory of Target Vulnerability Assessment, Defense Engineering Institute,AMS,PLA+YSX2024KFXY005.

**Author's Contribuitions:** Conceptualization, Guanghao Shi; Investigation, Guanghao Shi and Zhengxiang Huang; Writing-original draft, Guanghao Shi; Methodology, Guanghao Shi; Test technical support, Zhengxiang Huang; Writing-review & editing, Guanghao Shi and Zhengxiang Huang; Supervision, Zhengxiang Huang; Funding acquisition, Zhengxiang Huang

**Data Availability:** Research is only available upon request

**Editor:** Marcílio Alves

## References

Bockheim J G, Mazhitova G, Kimble J M, et al. Controversies on the genesis and classification of permafrost-affected soils[J]. Geoderma, 2006, 137(1-2): 33-39.

Bragov A M, Balandin V V, Igumnov L A, et al. Impact and penetration of cylindrical bodies into dry and water-saturated sand[J]. International Journal of Impact Engineering, 2018, 122: 197-208.

Feng J, Li W, Wang X, et al. Dynamic spherical cavity expansion analysis of rate-dependent concrete material with scale effect[J]. International Journal of Impact Engineering, 2015, 84: 24-37.

Forrestal M J, Longcope D B, Norwood F R. A model to estimate forces on conical penetrators into dry porous rock[J]. 1981.

Forrestal M J, Luk V K. Penetration into soil targets[J]. International Journal of Impact Engineering, 1992, 12(3): 427-444.

Forrestal M J, Tzou D Y. A spherical cavity-expansion penetration model for concrete targets[J]. International Journal of Solids and Structures, 1997, 34(31-32): 4127-4146.

Forrestal M J. Penetration into dry porous rock[J]. International Journal of Solids and Structures, 1986, 22(12): 1485-1500.

He T, Wen H M, Guo X J. A spherical cavity expansion model for penetration of ogival-nosed projectiles into concrete targets with shear-dilatancy[J]. Acta Mechanica Sinica, 2011, 27(6): 1001-1012.

KONG Lingming, ZHANG Haibing, SHEN Chunting, QI Jilin. UH model considering cryogenic intergranular suction for frozen saturated soil[J]. *Journal of Glaciology and Geocryology*, 2023, 45(3): 1063-1079.

Luk V K, Forrestal M J. Penetration into semi-infinite reinforced-concrete targets with spherical and ogival nose projectiles[J]. International Journal of Impact Engineering, 1987, 6(4): 291-301.

Satapathy S. Dynamic spherical cavity expansion in brittle ceramics[J]. International Journal of Solids and Structures, 2001, 38(32-33): 5833-5845.

Shi C, Wang M, Li J, et al. A model of depth calculation for projectile penetration into dry sand and comparison with experiments[J]. International Journal of Impact Engineering, 2014, 73: 112-122.

Shi G, Huang Z, Zu X, et al. Theoretical and experimental investigation of shaped charge jet penetration in soil targets with varying moisture content[J]. Granular Matter, 2026, 28(2): 27.

Wood D M. Soil behaviour and critical state soil mechanics[M]. Cambridge university press, 1990.

YAO Yang-ping. Advanced UH models for soils[J]. Chinese Journal of Geotechnical Engineering, 2015, 37(2): 193-217.

Zhu Q, Huang Z, Xiao Q, et al. Theoretical considerations on cavity diameters and penetration depths of concrete materials generated by shaped charge jets using the targets response modes described by a modified HJC model[J]. International Journal of Impact Engineering, 2020, 138: 103439.